BUTTERWORTH HEINEMANN

Coherent vortices in thermally stratified and rotating turbulence

O. Métais and M. Lesieur
Laboratoire des Ecoulements Géophysiques et Industriels (URA CNRS 1509), Institut de Mécanique de Grenoble, Institut National Polytechnique de Grenoble, and Université Joseph Fourier, Grenoble, France

Developed turbulent flows contain coherent vortices of various sizes, which play a major role in heat and mass transfer processes. We present here results of direct and large-eddy simulations LES focusing on the role played by these coherent vortices. We describe in detail the formalism of large-eddy simulations of turbulence, with a family of models developed on the basis of Kraichnan's eddy-viscosity. We see, for example, how longitudinal hairpin vortices are taken into account within these LES. We discuss vortex structure identification. Various results are presented concerning large-scale intermittency of a passive temperature and the role played by a stable-stratification to reduce this intermittency. We show numerical simulations of separated flows (backstep flow) with and without stratification, demonstrating the ability for LES to deal with complex geometries. Finally, the influence of solid-body rotation on free-shear flows is investigated, showing drastic modification of the flow topology.

Keywords: large-eddy simulation; turbulence; coherent vortices; intermittency; separated flows; rotation

Large-eddy simulations: formalism

Direct numerical simulations of turbulence (DNS) consist in explicitly solving all the scales of motion, from the largest l_I to the Kolmogorov dissipative scale l_D. It is well known from the statistical theory of turbulence that l_I/l_D scales like $R_I^{3/4}$, where R_I is the large-scale Reynolds number $u'l_I/\nu$ based upon the rms velocity fluctuation u'. Therefore, the total number of degrees of freedom necessary to represent the whole span of scales of a three-dimensional 3-D turbulent flow is of the order of $R_I^{9/4}$ in three dimensions. With the computers presently available, the DNS are then limited to Reynolds numbers several orders of magnitude smaller than those encountered in the atmosphere, the ocean, or most of industrial facilities. To increase the Reynolds number in the simulations, it is necessary to introduce a subgrid-scale model representing the action of scales smaller than Δx — the computational mesh — upon the explicitely resolved scales. The formalizm of the large-eddy simulations for incompressible flows is the following: consider a spatial filter G of width Δx, which filters out the *subgrid scales* of wavelength $< \Delta x$. The filtered field is defined as follows:

$$\bar{u}_i(\mathbf{x}, t) = \int u_i(\mathbf{y}, t)G(\mathbf{x}-\mathbf{y})\,d\mathbf{y} = \int u_i(\mathbf{x}-\mathbf{y}, t)G(\mathbf{y})\,d\mathbf{y} \tag{1}$$

and the subgridscale field is the departure of the actual flow with respect to the filtered field:

$$u_i = \bar{u}_i + u_i' \tag{2}$$

Address reprint requests to Dr. Oliver Métais, Laboratoire des Ecoulements Géophysiques et Industriels, Institut de Mécanique de Grenoble, Institut National Polytechnique de Grenoble, B.P. 53, F-38041 Grenoble Cedex 9, France.

Received 24 January 1995; accepted 30 May 1995

Because of the commutative properties of the filter and the derivatives, the continuity equation $\partial\bar{u}_j/\partial x_j = 0$ for the filtered field still holds. We now consider the incompressible Navier–Stokes equations within the Boussinesq approximation, in a frame rotating with constant angular velocity Ω about the x_3 axis, and apply the filter G to the equations. It is obtained:

$$\frac{\partial\bar{u}_i}{\partial t} + \frac{\partial}{\partial x_j}(\bar{u}_i\bar{u}_j) = -\frac{1}{\rho_0}\frac{\partial\bar{p}}{\partial x_i} + 2\epsilon_{ij3}\Omega\bar{u}_j - \beta g_i\delta_{i3}(\bar{T}-T_0) + \frac{\partial}{\partial x_j}\left\{\nu\left(\frac{\partial\bar{u}_i}{\partial x_j}+\frac{\partial\bar{u}_j}{\partial x_i}\right) + T_{ij}\right\} \tag{3}$$

$$\frac{\partial\bar{T}}{\partial t} + \frac{\partial}{\partial x_j}(\bar{T}\bar{u}_j) = \frac{\partial}{\partial x_j}\left\{\kappa\frac{\partial\bar{T}}{\partial x_j} + R_{ij}\right\} \tag{4}$$

T is the temperature, and $\bar{p}$ a filtered pressure including the geopotential; β is the fluid expansivity, taken equal to zero for passive scalar. T_{ij} and R_{ij} are the subgrid-scale transfers:

$$T_{ij} = (\bar{u}_i\bar{u}_j - \overline{u_iu_j}) \tag{5}$$

$$R_{ij} = (\bar{T}\bar{u}_j - \overline{Tu_j}) \tag{6}$$

Similarly to the Reynolds equations, an eddy–viscosity and eddy–diffusivity assumption is performed for modeling the subgrid fluxes, namely:

$$T_{ij} = \nu_t\left(\frac{\partial\bar{u}_i}{\partial x_j}+\frac{\partial\bar{u}_j}{\partial x_i}\right) + \frac{1}{3}T_{ll}\delta_{ij} \tag{7}$$

$$R_{ij} = \kappa_t\frac{\partial\bar{T}}{\partial x_j} \tag{8}$$

Here, we present several commonly used subgrid-scale models. Most of these are based upon an analogous mixing-length

Int. J. Heat and Fluid Flow 16: 315–326, 1995

655 Avenue of the Americas, New York, NY 10010

0142-727X/95/$10.00
SSDI 0142-727X(95)00044-Q

assumption consisting in writing $\nu_t \sim \Delta x\, v_{\Delta x}$, where $v_{\Delta x}$ is a characteristic velocity scale of the motions of size $\approx \Delta x$. Furthermore, the models generally depend upon one constant which can be analytically derived if it is assumed that the cut-off spectral wave number $k_C = \pi/\Delta x$ is located within a Kolmogorov kinetic energy cascade, so that:

$$E(k) = C_K \epsilon^{2/3} k^{-5/3} \tag{9}$$

where $E(k)$ is the kinetic energy spectrum and C_K is the Kolmogorov constant.

Smagorinsky's model

The first of these subgrid models was proposed by Smagorinsky (1963) for numerical studies related to a two-layer quasi-geostrophic atmosphere. It consists in writing

$$\nu_t \sim \Delta x\, v_{\Delta x} \sim (\Delta x)^2 \frac{\partial v}{\partial x} = (C_S \Delta x)^2 \bar{S}^{1/2} \tag{10}$$

where $v_{\Delta x}$ is a characteristic velocity difference on the computational grid mesh, determined by the local strain

$$\bar{S} = \frac{1}{2}\left(\frac{\partial \bar{u}_i}{\partial x_j} + \frac{\partial \bar{u}_j}{\partial x_i}\right)\left(\frac{\partial \bar{u}_i}{\partial x_j} + \frac{\partial \bar{u}_j}{\partial x_i}\right) \tag{11}$$

For π/Δ_x situated within a Kolmogorov cascade, it is obtained:

$$C_S = \frac{1}{\pi}\left(\frac{3C_K}{2}\right)^{-3/4} \sqrt{\frac{\langle \bar{S} \rangle^{3/2}}{\langle \bar{S}^{3/2} \rangle}} \tag{12}$$

If the Kolmogorov constant is chosen equal to 1.4, which corresponds to a frequently measured value (see, e.g., Saddoughi and Veeravalli 1994), Equation 12 then gives $C_S \approx 0.18$, assuming a strain ratio of unity.

This model was used in particular by Deardorff (1970) and Moin and Kim (1982) for the channel flow (with $C_S = 0.1$ and appropriate wall laws), and since then, in many of the large-eddy simulations of engineering flows. For 3-D isotropic turbulence, Smagorinsky's model (with $C_S = 0.18$) behaves acceptably, although the kinetic energy spectrum decays faster than with the structure-function model (see Métais and Lesieur 1992). However, Smagorinsky's model is too dissipative in the presence of a boundary and does not work for transition in a boundary-layer on a flat plate, starting from a laminar profile to which a small perturbation is superposed.

We now present other subgrid-scale models, based on the concept of Kraichnan's eddy–viscosity.

Spectral eddy–viscosity models

We assume that we work in the Fourier space, in the context of 3-D isotropic turbulence. The filter consists in a sharp cut-off filter clipping all the modes larger than k_C, where $k_C = \pi/\Delta x$ is the cut-off wave number. The concept of k-dependent eddy–viscosity was introduced by Kraichnan (1976) for 3-D isotropic turbulence in the following way. If $T_{>k_C}(k, t)$ is the kinetic energy transfer across the cutoff k_C, corresponding to triadic interactions so that $k < k_C$, p and (or) $q > k_C$ (see Lesieur 1990 for details), one poses

$$\nu_t(k \mid k_C) = -\frac{T_{>k_C}(k, t)}{2k^2 E(k, t)} \tag{13}$$

in such a way that the kinetic energy spectrum $E(k, t)$ in the resolved scales ($k \leqslant k_C$) satisfies:

$$\left[\frac{\partial}{\partial t} + 2\big(\nu + \nu_t(k \mid k_C)\big)k^2\right] E(k, t) = T_{<k_C}(k, t) \tag{14}$$

where $T_{<k_C}(k, t)$ is the kinetic energy transfer corresponding to resolved triads so that $k, p, q \leqslant k_C$. The kinetic energy transfers can be derived from the Eddy-Damped Quasi-Normal Markovian (E.D.Q.N.M.) theory, one of the statistical closures of isotropic turbulence (see Lesieur). We assume first that k and k_C lie within a Kolmogorov cascade, and $k \ll k_C$. Then the transfer $T_{>k_C}(k, t)$ across k_C can be analytically determined with the aid of expansions in powers of the small parameter k/k_C. This yields:

$$\nu_t^{\infty} = 0.441 C_K^{-3/2} \left[\frac{E(k_C)}{k_C}\right]^{1/2} \tag{15}$$

where $E(k_C)$ is the kinetic energy spectrum at the cutoff k_C. For k close to k_C, $T_{>k_C}(k, t)$ has to be evaluated using the E.D.Q.N.M. approximation. It still scales on $[E(k_C)/k_C]^{1/2}$ but with a coefficient rising rapidly in the neighborhood of k_C (cusp behavior). Notice that the scaling by $[E(k_C)/k_C]^{1/2}$ may be obtained by a mixing-length argument, where the eddy–viscosity is proportional to the product of k_C^{-1} by the characteristic turbulent velocity $v(k_C)$. The latter is itself proportional to $\sqrt{k_C E(k_C)}$. The analysis also allows us to introduce a spectral eddy–diffusivity, with the same behavior as the eddy–viscosity (plateau and cusp), with a turbulent Prandtl number Pr_t approximately constant. Note that the latter varies with the adjustable constants of the E.D.Q.N.M. theory (see Lesieur). Chollet and Lesieur (1982) choose the constants so that $\mathrm{Pr}_t = 0.6$ in agreement with experimental measurements (see, e.g., Champagne et al. 1977).

This spectral cusp eddy–viscosity may be used in large-eddy simulations performed in spectral space, provided the kinetic energy spectrum at the cutoff can be determined. Good results are obtained for decaying isotropic turbulence (see Lesieur and Rogallo 1989; Métais and Lesieur 1992). The model works well even if the large scales are not isotropic, as was shown by Métais and Lesieur and Batchelor et al. (1992) for stably stratified turbulence. It gives also interesting results for temporal mixing layers, in terms of Kelvin–Helmholtz vortices dynamics, stretching of hairpin vortices, and helical pairings (Silvestrini et al. 1995).

However, such an eddy–viscosity is difficult to employ if we want to work directly in physical space, when the geometry of the problem prevents spectral methods to be used. An alternative method is to define an *average* spectral eddy–viscosity, using energy conservation arguments:

$$\int_0^{k_C} 2\nu_t^{av}(t) k^2 E(k, t)\, \mathrm{d}k = \epsilon(t) \tag{16}$$

It yields (see Métais and Lesieur 1992)

$$\nu_t = \frac{2}{3} C_K^{-3/2} \left[\frac{E(k_C)}{k_C}\right]^{1/2} \tag{17}$$

This is, in fact, very close to Smagorinsky's model and to the model proposed by Yakhot and Orszag (1986) on the basis of a mixed E.D.Q.N.M./Renormalization Group (RNG) theory.

Structure–function model

This model, from Métais and Lesieur (1992), is an attempt to use the spectral eddy–viscosity in physical space, while taking into account the intermittency of turbulence. The eddy–viscosity given by Equation 17 can be determined locally in physical space, if a local kinetic energy spectrum $E_x(k_C)$, with $k_C = \pi/\Delta_x$ can be defined. This can be done using the local second-order velocity structure function

$$\bar{F}_2(\mathbf{x}, \Delta x, t) = \langle \| \mathbf{u}(\mathbf{x}, t) - \mathbf{u}(\mathbf{x} + \mathbf{r}, t) \|^2 \rangle_{\|\mathbf{r}\| = \Delta x} \tag{18}$$

For a uniform grid, the average is done on the six closest points surrounding x on the computational grid. A 4-point version can also be used when there are preferential planes in the flow; for example, planes parallel to boundaries in a channel or a boundary layer. If the grid spacing is not uniform, extrapolations can be performed using the fact that, in a 3-D Kolmogorov cascade, the second-order velocity structure function between two points a distant r apart scales like $r^{2/3}$. Using isotropic turbulence relations, such as

$$\bar{F}_2(\mathbf{x}, \Delta x, t) = 4\int_0^{k_c} E(k)\left(1 - \frac{\sin(k\Delta x)}{k\Delta x}\right) \mathrm{d}k$$

it is obtained within a Kolmogorov spectrum

$$\nu_t(\mathbf{x}, \Delta x, t) = 0.105 C_K^{-3/2} \Delta x \left[\bar{F}_2(\mathbf{x}, \Delta x, t)\right]^{1/2} \tag{19}$$

Notice that in the limit $\Delta x \to 0$, and for a regular mesh, we can write:

$$\bar{F}_2(\mathbf{x}, \Delta x, t) \approx \frac{1}{3}\Delta x^2 \left(\frac{\partial u_i}{\partial x_j}\right)\left(\frac{\partial u_i}{\partial x_j}\right) = \frac{1}{6}\Delta x^2 \left[\bar{S} + \bar{\omega}\bar{\omega}\right]^{1/2} \tag{20}$$

where $\bar{S}$ is defined by Equation 11 and $\boldsymbol{\omega}$ is the large-scale vorticity vector. Equations 19 and 20 yield:

$$\nu_t(\mathbf{x}, \Delta x, t) \approx \frac{0.105}{\sqrt{6}} C_K^{-3/2} \Delta x^2 \left[\bar{S} + \bar{\omega}\bar{\omega}\right]^{1/2} \tag{21}$$

Noticing that $0.105\ C_K^{-3/2} \approx 2C_S^2$ (C_S Smagorinsky's constant), we finally obtain

$$\nu_t(\mathbf{x}, \Delta x, t) \approx \sqrt{\frac{2}{3}}\,(C_S \Delta x)^2 \left[\bar{S} + \bar{\omega}\bar{\omega}\right]^{1/2} \tag{22}$$

As compared to Smagorinsky's model, the turbulent viscosity given by the structure function model acts more in regions of high vorticity and low strain. Conversely, its action is less pronounced in regions of high strain and low vorticity.

This model works very well for isotropic turbulence, where it gives a good Kolmogorov spectrum at the cutoff. This is shown in Figure 1, displaying the compensated kinetic energy spectrum $\epsilon^{-2/3}k^{5/3}E(k, t)$ in a decaying isotropic LES, at a resolution of 96^3. the compensated spectrum is fairly constant (with a Kolmogorov's constant C_K of 1.4) from $k = 10$ to $k = 40$. In the same figure, we have reported the pressure spectrum E_{pp}, compensated according to Batchelor's law

$$E_{pp}(k, t) = C_P \epsilon^{4/3} k^{-7/3} \tag{23}$$

This law can be obtained using the quasinormal approximation for the determination of the second-order moment for pressure $\langle \hat{p}(\mathbf{k})\hat{p}(\mathbf{k}')\rangle$. The constant C_P was calculated by Monin and Yaglom (1975). They found $C_P = \alpha C_K^2$ with

$$\alpha = \frac{7}{3}\left(\frac{27}{55}\right)^2 \frac{\Gamma\left(\frac{1}{3}\right)^2}{\Gamma\left(-\frac{4}{3}\right)} \approx 1.32 \tag{24}$$

In the figure, there is a tiny plateau of the compensated pressure spectrum at the right value C_P corresponding to $C_K = 1.4$. Higher resolution computations should be performed to investigate the nature of the pressure spectrum within the inertial range of 3-D isotropic incompressible turbulence.

The structure–function model gives also interesting results for free-shear flows (see the wake of Figure 5), and backstep flow (see Figures 8 and 9). It works well also for rotating turbulence

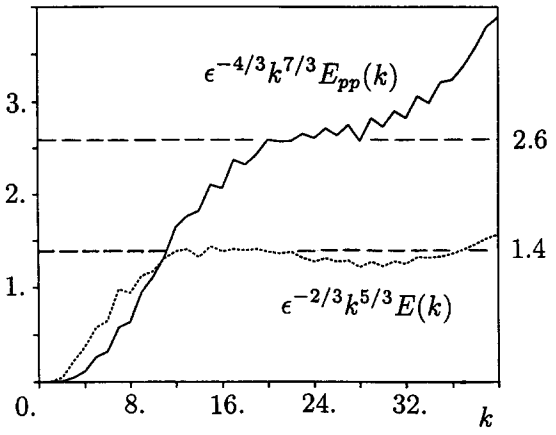

Figure 1 LES (structure–function model) of decaying turbulence; compensated kinetic energy and pressure spectra (from Métais and Lesieur 1992)

(see Bartello et al. 1994). It permits, within the 4 point formulation, simulation of the transition on a periodic flat plate at Mach 4.5 (see Ducros et al. 1993). However, it still does not work for transition on a wall at low Mach, because the eddy–viscosity reacts to the presence of *TS* waves enough to prevent them from developing into turbulence.

Selective and filtered structure–function models

The selective structure–function (SSF) model was developed by David (1993) (see Comte et al. 1994; Lesieur and Métais 1995 for details). The idea is to switch off the eddy–viscosity when the flow is not 3-D enough. The three-dimensionalization criterion is the following: measure the angle between the vorticity at a given grid point and the average vorticity at the six closest neighboring points (or the four closest points in the 4-point formulation). If this angle exceeds 20°, the most probable value according to simulations of isotropic turbulence at a resolution of $32^3 \sim 64^3$, the eddy–viscosity is turned on. Otherwise, there is only molecular dissipation which acts. This model works very well for isotropic turbulence and free-shear flows. We will show below an application to a stably stratified flow above a backward-facing step.

The SSF model was also used to simulate a compression ramp at Mach 2.5 by David (1993). The SSF simulations predicted the existence of longitudinal Görtler-type vortices.

In the filtered structure–function (FSF, see Ducros et al. 1993; see also Comte et al. 1994; Lesieur and Métais 1995), the filtered field $\bar{u}_i$ is submitted to a high-pass filter in order to get rid of low-frequency oscillations which affect the local kinetic energy spectrum $E(k_C)$ in Equation 17. The model works well for both isotropic turbulence and transition in a spatially developing boundary layer.

Dynamic models

This class of models, still in progress, is based on Germano's (1992) work (see also Germano et al., 1991 and Lesieur and Métais 1995, for a review). A new filter $\langle . \rangle$ (called the test filter, generally of width $2\Delta x$) is applied to $\bar{u}$, giving a "test-field" $\langle \bar{u} \rangle$. The evaluation of the energetic transfers between the test field and $\bar{u}$, based on the so-called Germano's identity, permits us in principle, to recalculate a time-varying Smagorinsky's constant $C = C_S^2$ which is local in space. However, the problem is ill-conditioned, since C is given by a tensorial equation

yielding five equations for one unknown. This is why, in the channel-flow simulations carried out in Germano et al., they have to average C in planes parallel to the boundary. Good results are thus obtained. To remove the singularity, Lilly (1992) proposed to evaluate C by variational techniques, via a least-square approach. However, this yields many negative values for $C(\mathbf{x}, t)$, which rapidly lead to computational instability. The cure often adopted to deal with this problem consists in averaging over direction of flow homogeneity. For example, Germano et al. and Piomelli (1993) obtained very good results by averaging in planes parallel to the walls in their channel flow simulation. Note that the use of Smagorinsky's model as a base for the dynamic procedure is not compulsory, and any of subgrid-scale models can be a candidate. As example, Zang et al. (1993) have successfully utilized this procedure to the scale-similarity model proposed by Bardina et al. (1980). More recently, El-Hady and Zang (1995) have shown that the "dynamic" structure-function model yields better results than the "dynamic" Smagorinsky model in transitional compressible boundary layer.

An approach having similarities with the dynamic model procedure has been proposed in spectral space (Lesieur and Rogallo 1989): an LES of decaying isotropic turbulence using the spectral eddy–viscosity (with cusp) was carried out, with a cutoff k_C. Then the explicit transfers across $k_C/2$, added to the modeled transfers across k_C, permitted to recalculate the constants of the model (level of the plateau and shape of the cusp). Unfortunately, the method, once iterated, did not converge.

Coherent vortices identification

It is now well accepted that developed turbulent flows contain a lot of coherent vortices of various sizes, which play a major role in all heat and mass transfer processes. These vortices, which correspond to local concentrations of vorticity $\boldsymbol{\omega} = \boldsymbol{\nabla} \times \boldsymbol{u}$ in space, are present in isotropic 2- and 3-D turbulence, and in free-shear flows such as mixing layers, wakes, jets, and separated flows. They can also be found in flows close to boundaries, such as boundary layers, channel flows, or pipe flows. To define a coherent vortex, we think it is important to include the notion of time evolution.

We consider at some time a region of space with a local concentration of vorticity ω. This region is supposed to move at a velocity U_c. It will be said to be a coherent vortex if it exhibits a distinctive shape and if it has a life time T_c much larger than the local turnover time within the eddy, ω^{-1} (say, $\approx 5\omega^{-1}$). We follow the isolated vortex in a Galilean frame moving with a constant velocity of the order of U_c. Consideration of the order of magnitude of the different terms of the equation of motion (in the constant-density case, and neglecting viscosity) shows that the vorticity $\boldsymbol{\omega}$, the velocity $\boldsymbol{u}$ (induced by the vortex), and the generalized dynamic pressure P satisfy, in a coherent vortex, the cyclostrophic balance

$$\boldsymbol{\omega} \times \mathbf{u} = -\frac{1}{\rho}\boldsymbol{\nabla} P \tag{25}$$

This shows that the pressure gradient is oriented toward the exterior of the vortex: the center of the coherent structure is a pressure trough.

The fact that low-pressure regions are good indicator of the coherent vortices is revealed through examination of the pressure probability density function (pdf). Figure 2 shows the pressure pdf as given by a direct numerical simulation of decaying 3-D isotropic turbulence at a resolution of 128^3. The pdf exhibits a very asymmetric shape, with an exponential fit in the lows. Conversely, the high pressure one is very close to Gaussian. This is a clear signature of highly concentrated coherent vortices: the

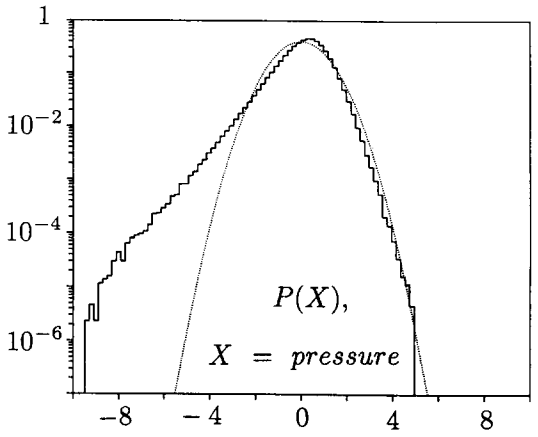

Figure 2 DNS of 3-D decaying turbulence; pressure probability density function compared to a Gaussian distribution of same variance (dots)

flow is composed of very localized regions of strong depression. Concentrated low-pressure structures are still present in large-scale simulations of 3-D isotropic turbulence (see Métais and Lesieur 1992). In that case, the low-pressure regions are better indicators of the coherent vortices than the high-vorticity regions, which are very scattered. Similarly skewed pdf have been observed in the direct numerical simulations of mixing layer performed by Comte et al. (1992). These have also been measured in experimental swirling turbulent flows.

We now consider the effect of a solid body rotation of angular velocity $\boldsymbol{\Omega}$. In this case, the coherent vortex satisfies

$$(\boldsymbol{\omega} + 2\boldsymbol{\Omega}) \times \boldsymbol{u} = -\frac{1}{\rho}\boldsymbol{\nabla} P \tag{26}$$

If rotation $\boldsymbol{\Omega}$ is fast, which can be measured in terms of the local Rossby number $R_o \ll 1$, with

$$R_o = \left| \frac{\omega}{2\Omega} \right| \tag{27}$$

Equation 26 is approximated by the geostrophic balance

$$2\boldsymbol{\Omega} \times \boldsymbol{u} = -\frac{1}{\rho}\boldsymbol{\nabla} P \tag{28}$$

which replaces the previous cyclostrophic balance. In this case, cyclonic vortices (of vorticity parallel and of same sign as $\boldsymbol{\Omega}$) will correspond to pressure lows, while anticyclonic vortices will be pressure highs.

Thermal intermittency

Here we present results of LES and DNS of 3-D isotropic turbulence convecting a passive scalar ("temperature") at a resolution of 128^3. We have also examined the case of the nonpassive temperature in the presence of stable stratification.

In the isotropic case (with a passive temperature), we found that the temperature exhibits several *anomalous* characteristics, as compared with the predictions of classical theories. Figure 3 shows the kinetic energy and temperature spectra obtained after several (60) large-eddy turnover time in a large-eddy simulation using the previously described Kraichnan spectral-cusp eddy–viscosity and eddy–diffusivity (turbulent Prandtl number of 0.6). Initially ($t = t_0$), both velocity and temperature are independent Gaussian fields with identical spectra.

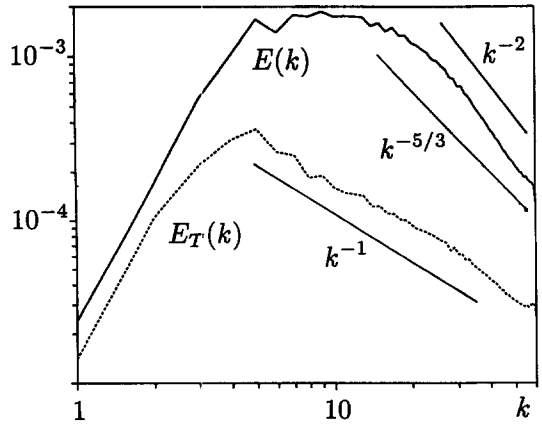

Figure 3 LES of 3-D decaying turbulence; kinetic energy spectrum $E(k)$ and passive-temperature spectrum $E_T(k)$ after 60 large-eddy turnover times (from Métais and Lesieur 1992).

Figure 3 shows that the temperature has decayed much faster than the kinetic energy, with a peak migrating faster toward low wavenumbers. The kinetic energy spectrum at the cutoff is close to $k^{-5/3}$, with a Kolmogorov constant, measured from the compensated spectrum $k^{5/3}E(k)$, of the order of 1.5. However, the kinetic energy seems somewhat constrained by k_c, resulting in a slope close to k^{-2} in the vicinity of k_c. The temperature spectrum agrees quite well with Corrsin–Oboukov's law $E_T(k) \sim \eta\epsilon^{-1/3}k^{-5/3}$ at the cutoff (where η is the temperature variance dissipation rate), with a constant equal to 0.9. However, the most striking feature of this spectrum is the formation, for $k < 30$, of a range close to a k^{-1} power law (see Métais and Lesieur 1992; Lesieur and Rogallo 1989). Afterwards we consider the thermal 3-D structures. It is well known, since the work of Siggia (1981) (see also She et al. 1990; Vincent and Meneguzzi 1991; Métais and Lesieur), that coherent vortices exist in 3-D isotropic turbulence. They have the form of thin elongated tubes of high vorticity and low pressure. In our DNS, we find that the length of such vortices is of the order of the integral scale of turbulence l, while their diameter seems to scale on Taylor's microscale, and their respective distance is $\approx 2l$. We have checked (see Métais and Lesieur) that the high-temperature fluctuations are strained in the "braid" region between the coherent vortex tubes. The same occurs in 2-D turbulence where the temperature is strained between the large coherent vortices. In the inertial–convective range of 2-D turbulence, the kinetic energy spectrum is $\propto k^{-3}$ (enstrophy cascade), while the temperature spectrum is proportional to the enstrophy spectrum, and therefore $\propto k^{-1}$ (see Lesieur and Herring 1985). In Lesieur and Rogallo (1989), the large scale k^{-1} range was explained assuming that the temperature flux η was controlled by the rate ϵ/u^2 (u rms velocity) imposed by the shear in the energetic scales: $\eta \sim E_T(k)\epsilon/u^2$ ($E_T(k)$ temperature variance spectrum). This is exactly a 2-D inertial–convective argument in the enstrophy cascade, where the shearing rate is constant and equal to $\beta^{1/3}$ (β is the enstrophy dissipation rate, see Lesieur 1990).

As in 2-D turbulence, the large-scale intermittency will be responsible for the highly non-Gaussian pdf of the vorticity. Since high concentrations of temperature are in between the vortices, it is natural to expect that the temperature pdf at large amplitudes will follow the vorticity. Therefore, we have examined the pdf for both velocity and temperature fields and their derivatives after 17 large-eddy turnover times (DNS and LES). We introduce the skewness (S) and flatness factors (F) of the distribution f: $S_f = \langle f^3\rangle/\langle f^2\rangle^{3/2}, F_f = \langle f^4\rangle/\langle f^2\rangle^2$. As observed in grid turbulence experiments, the velocity pdf is close to Gaussian ($S_u \approx 0$; $F_u \approx 3$). However, T exhibits near exponential ranges in the wings of its distribution (see Figure 4): the temperature-variance flatness is 4. As previously mentioned, this departure from Gaussianity for the temperature fluctuation pdf indicates a large-scale intermittency. Indeed, the temperature presents very strong fluctuations in small spatial regions, with quiescent regions being more likely the result of random sampling. Pronounced exponential tails for the pdf of the passive temperature fluctuations have been observed experimentally by Jayesh and Warhaft (1992). However, this intermittent behavior was only observed in the presence of a nonzero mean temperature gradient. In the absence of gradient, the experimental temperature pdf are close to Gaussian. This apparent discrepancy between the present numerical results and the experimental observation is still an open issue. Small-scale intermittency is illustrated by the distributions of the velocity and temperature derivatives (see Figure 4, for $\partial T/\partial x_3$ pdf). The departure from Gaussianity for the temperature derivative is more pronounced than for the velocity: $F_{\partial T/\partial x_3} = 5.47$ when $F_{\partial u/\partial x_3} = 4.59$. Larger values for the temperature derivative flatness, as compared with the velocity derivative flatness, are in good agreement with experimental measurements (Antonia et al. 1978; Sreenivasan et al. 1980).

Let us now consider a temperature no longer passive, but coupled to the velocity field by the presence of a mean stable temperature profile ($\beta \neq 0$ in Equation 3). We assume that the Brunt–Väisälä frequency N (N^2 proportional to the mean temperature profile) is constant. We also assume that the isotropic subgrid-scale modeling of momentum and temperature used for the passive scalar case is still valid in the stratified case, provided that turbulence should not depart too much from isotropy for

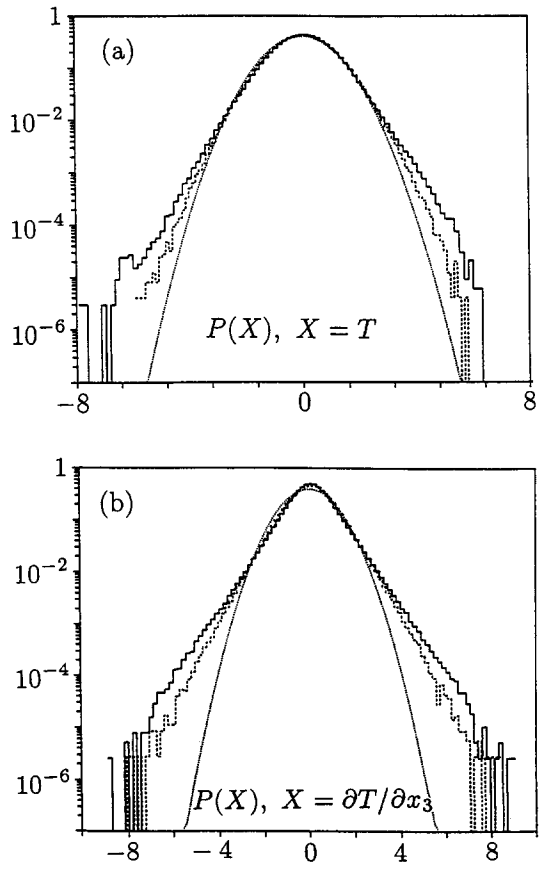

Figure 4 Probability density function $P(X)$: (a) $X = T$; (b) $X = \partial T/\partial x_3$; large eddy-simulation: dots; direct simulation: continuous line; dashed line corresponds to a Gaussian distribution of same variance (from Métais and Lesieur 1992)

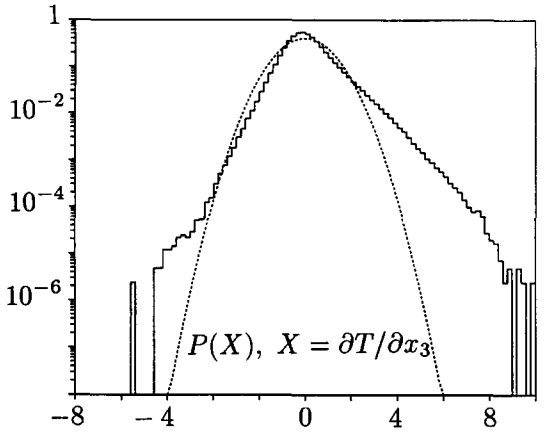

Figure 5 Probability density function of $\partial\tilde{T}/\partial x_3$, stably stratified direct simulation: $t = 1.233N^{-1}$; dashed line corresponds to a Gaussian distribution

$k > k_C$. We focus on weakly stratified turbulence for which the initial Froude number is not small ($F_r = 1.3$) and whose statistical kinematic properties are almost unchanged as compared to the passive temperature case. Due to the coupling, the temperature spectrum has lost the anomalous character it had in the passive case and looks quite similar to the kinetic energy spectrum with a behavior close to $k^{-5/3}$. Furthermore, both velocity and temperature fluctuations pdf now exhibit a Gaussian behavior (see Métais and Lesieur 1992). This indicates the disappearance of large-scale temperature intermittency. Figure 5 shows the pdf for $\partial\tilde{T}/\partial x_3$($\tilde{T}$ temperature deviation from the mean temperature profile) obtained in a direct Boussinesq simulation at $Pr = 1$ and $F_r = 1.3$ (see Métais and Lesieur, for details). The pdf exhibits a very asymmetrical shape with a skewness factor of 1.027. This is confirmed by the experimental data of Thoroddsen and Van Atta (1993). A possible explanation is that locally large negative values of $\partial\tilde{T}/\partial x_3$ are convectively unstable and, therefore, rapidly destroyed by buoyancy forces; whereas, large positive values enhance stability and, therefore, tend to persist.

Free-shear flows

Plane wake: temporal growth

We first assume periodicity in the stream-wise direction (temporal hypothesis) and in the span-wise direction. The initial conditions consist of a Gaussian mean velocity profile:

$$\bar{u}(y) = U_m \exp\left[-(\log 2)\frac{y^2}{r_m^2}\right] \tag{29}$$

where r_m is the half deficit velocity width, to which a low-amplitude random perturbation is superposed. The latter results from the superposition of two random perturbations: the first one is 2-D (independent of the span-wise direction) of kinetic energy $\epsilon_{2D}U_m^2$, and the second one is 3-D of kinetic energy $\epsilon_{3D}U_m^2$, with $\epsilon_{2D} = 10^{-4}$ and $\epsilon_{3D} = 10^{-5}$. The initial perturbation is therefore quasibidimensional. The resolution is $48 \times 48 \times 48$ collocations points (pseudospectral method).

We compare the coherent vortices respectively obtained in a direct numerical simulation (Figure 6a) at Reynolds $R_e = U_m r_m/\nu = 200$, and in large-eddy simulations using various subgrid-scale models (no molecular viscosity). The initial conditions are identical in all cases. We have successively considered the *structure function model* given by Equation 19 in the 6-point formulation (Figure 6b), the classical Smagorinsky model given by Equation 10 with $C_S = 0.18$ (Figure 6c). For each case, we visualize an isosurface of the vorticity modulus: $\omega = 0.5\omega_i$ (ω_i is the vorticity maximum associated with the initial mean velocity profile) at time $t = 76r_m/U_m$. The length of the computational domain is twice the most amplified wavelength predicted by the linear-stability analysis: the Karman-street consists of two pairs of alternate sign vortices (see Figure 6a). At low Reynolds number (Figure 6a), the Karman rolls exhibit some oscillations in the span-wise direction but the longitudinal vorticity component remains small with respect to the span-wise one ($\approx 10\%$). The three-dimensionality is greatly enhanced in the case of large-eddy simulations. Figure 6b shows that the primary vortices of the Karman street are still present but vortex stretching leads to the formation of intense counter-rotating vortices between the span-

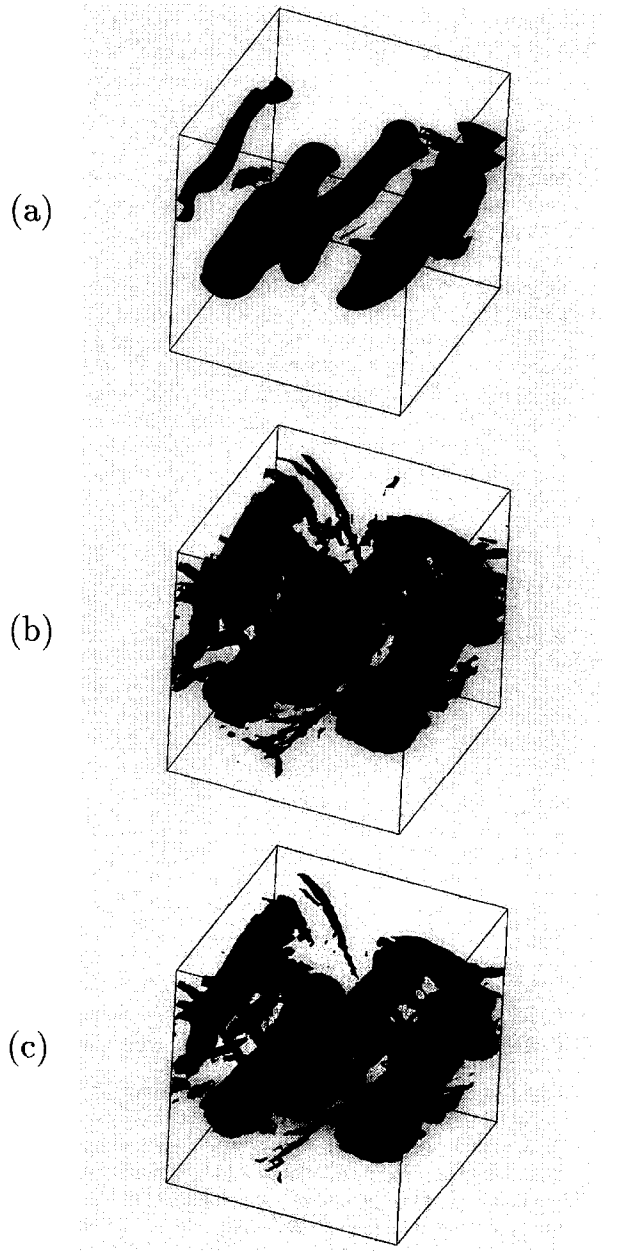

Figure 6 Vorticity modulus isosurface $\omega = 0.5\omega_i$ at $t = 76r_m/U_m$: (a) direct numerical simulation at $R_e = U_m r_m/\nu = 200$; large-eddy simulations; (b) structure-function model; (c) Smagorinsky's model with $C_S = 0.18$

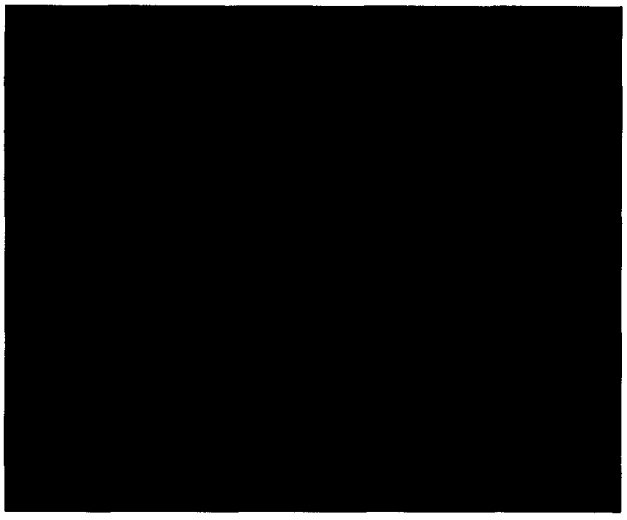

Figure 7 Large-eddy simulation of a spatially developing plane wake: structure–function model; vorticity modulus isosurface $\omega = 90\%\omega_i$ (from Gonze 1993)

wise ones. These longitudinal structures are located within the braids connecting consecutive Karman vortices of antiparallel vorticity. At that time, $\omega_{max} = 2.22\omega i$, where ω_{max} is the maximum intensity of the longitudinal vorticity component. We have checked that both the primary Karman vortices and the secondary longitudinal hairpin vortices correspond to pressure lows. Smagorinsky's model turns out to be more dissipative than the structure-function model leading to slightly lower values for the longitudinal vorticity component ($\omega_{max} = 2.13\omega i$; see Figure 6c). It is important to note that the LES preserve both the coherence of the Karman rollers and the thin longitudinal hairpin vortices whose diameter is close to the mesh size.

Plane wake: spatial growth

We have developed a 3-D numerical code combining, for the space derivatives computation, high-order difference schemes in the longitudinal direction and pseudospectral methods in the span-wise and shear directions. Compact difference schemes at the sixth order are used (Lele 1992). Their precision is close to spectral methods. This code allows us to simulate a spatially growing wake numerically, which is closer to experimental configurations.

Figure 7, taken from Gonze (1993), shows such a calculation using the *structure function* model (6 points). A deficit velocity profile steeper than Gaussian is imposed at the inflow to simulate a near-wake. We superpose small 3-D random perturbation ($\epsilon_{3D} \approx 10^{-4}$). The resolution is n_x, n_y, $n_x = 250$, 80, 48. Figure 7 visualizes the vorticity modulus $\omega = 90\%\omega_i$, where ω_i is the vorticity maximum associated with the mean velocity profile at the inlet. We still observe longitudinal stretching of hairpin vortices in the deformation field induced between counter-rotating Karman vortices. This stretching is more intense than in the temporal case, and the longitudinal vorticity maximum is $\omega_{max} = 4\omega_i$. A question arises concerning the relevance of these predictions with respect to actual wakes. An answer will be possible when sufficiently reliable experimental data concerning longitudinal vorticity exist. Computed statistics also need to be compared to measurements.

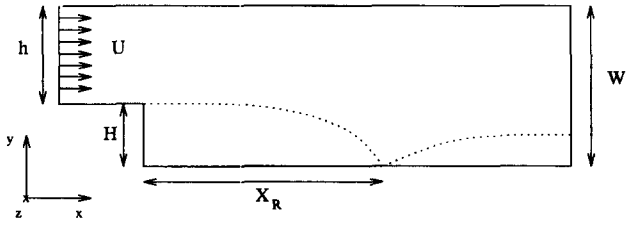

Figure 8 Schematic side view of the backward-facing step

Separated flows: backward-facing step

Here we focus on LES of a backward-facing step flow. The simulations use a finite-volume code (TRIO code) developed originally at the Atomic Energy Agency (CEA) in its center of Grenoble, for industrial modeling purposes. The code has been used at a high Reynolds number (Silveira-Neto et al. 1991, 1993) in a large-eddy simulation using the structure–function model (6-point formulation). Figure 8 shows a schematic side view of the apparatus. Let W/H be the aspect ratio, W being the channel height at the exit and H the step height. The Reynolds number is here UH/ν, where U is the velocity at the inlet.

In the case of a "high" step (aspect ratio of 1.25) and at a Reynolds number of 6,000, we find 2-D spiral eddies which stretch longitudinal hairpin vortices of vorticity $\approx 0.4\ \omega_{max}$. This is shown in Figure 9a at $t = 130H/U$ and on Figure 9b at $t = 138H/U$ taken from Silveira-Neto et al. (1993). In this simulation, the resolution is $130 \times 25 \times 40$. The incoming flow, supposed uniform, separates downstream of the step (left of the figure), and the resulting vortex sheet rolls up into Kelvin–Helmholtz billows which travel downstream and pair. The yellow and green filaments indicate the positive and negative longitudinal vorticity, corresponding to the stretched hairpin filaments.

A span-wise section of these vortices yields a typical mushroom-like structure, analogous to what had been observed experimentally and numerically in mixing layers. In fact, calculations at longer times and higher resolution show that the flow evolves eventually towards highly distorted Kelvin–Helmholtz billows more of the helical pairing type (see Comte et al. 1992), with weak Λ-shaped vortices shed downstream (Fallon 1994).

In the "low"-step case (aspect ratio 2.5, Reynolds 38,000), we present also a LES using the structure–function model. Visualizations of the vorticity field indicate the presence of

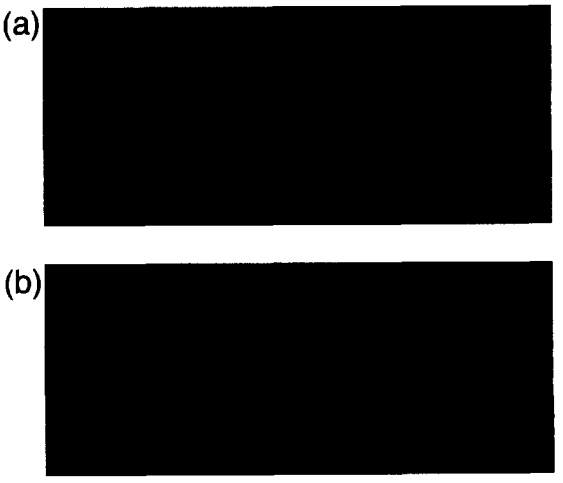

Figure 9 Span-wise and longitudinal vorticity in a backward-facing step flow simulation using the structure–function subgrid-scale model; high step (from Silveira-Neto et al. 1993): (a) $t = 130H/U$; (b) $t = 138H/U$

Figure 10 LES (with the structure-function model) of a backstep flow; low step, top view of the low-pressure field (from Silveira-Neto et al. 1993)

intense longitudinal vortices. However, the low-pressure field shows large depressions which might undergo some sort of helical pairing (see Figure 10). In these simulations at high Reynolds number, the reattachment length is equal to eight step heights, in very good agreement with the experiments. On the contrary, classical industrial models such as the $K-\epsilon$ model underestimate seriously this quantity, with a prediction of 6. Other statistics such as pressure coefficients and mean velocities compare also well with the experiments. The variances of the velocity components and the Reynolds stresses are also in good experimental agreement. In fact, in Silveira-Neto et al. (1993), these data were erroneously extrapolated assuming a subgrid Kolmogorov kinetic energy spectrum. Such a spectrum may occur only in the mixing layer close to the step, but not in the rest of the flow.

Stably stratified case

We have applied the structure-function (SF) and the selective structure-function (SSF) models to the backward-facing step (high-step case of aspect ratio 1.25) in a stably stratified medium at a Reynolds number 48,000 (see Fallon 1994 for details). The stratification is obtained by imposing a discontinuous temperature profile at the inlet above the step, so that: $T = T_2$ for $H \leqslant y \leqslant H + 0.2h$, and $T = T_1$ for $H + 0.2h \leqslant y \leqslant W$, with $T_1 > T_2$ (see Figure 8). The parameter characterizing the stratification strength is the global Richardson number defined as:

$$R_i = \beta g H (T_1 - T_2)/U_0^2 \qquad (30)$$

A parametric study by varying R_i has first been done with the SF model. In the weakly stratified case ($R_i < 0.25$) the coherent vortex topology is analogous to the isothermal case. When the stratification is increased ($R_i = 0.5$), the flow is two-dimensionalized upstream, with quasi-2-D Kelvin–Helmholtz vortices shed downstream of the step. Further downstream, however, they still undergo some highly 3-D pairing. The reattachment length is notably increased. Furthermore, the stretching of longitudinal hairpin vortices is strongly reduced. For $R_i = 0.7$, the mixing layer becomes purely 2-D, and the pairing is inhibited. The expansion rate of the mixing layer is dramatically reduced, and the reattachment length has become infinite. At $R_i = 1$, a very stable density interface forms, without any roll up.

To compare the SF and SSF models, we performed with the latter a simulation at $R_i = 0.7$. In fact, things are very different. Figure 11 shows the SSF simulation: vortices form immediately downstream of the step, and undergo several pairings. We can also observe baroclinic formation of smaller vortices in the braids, as had been found by Staquet (1991) in DNS of temporal stratified mixing layers. It is clear in these calculations that the SSF model treats 2-D instabilities better, since it has no influence on them. Therefore, it should be closer to reality than the SF model. This indicates that the SF model is too dissipative for 2-D vortices.

Rotating flows

Turbulent or transitional shear flows in a rotating frame play an important role in many geophysical and engineering applications. In these flows, the Rossby number (characterizing the relative importance of inertial over Coriolis forces) varies importantly. Typical values of the Rossby number are ≈ 0.05 in the mesoscale oceanic eddies, ≈ 0.3 for the large synoptic atmospheric perturbations, and ≈ 2.5 for the atmospheric wake of a small island. Rotating turbulence finds numerous industrial applications in turbomachinery: the turbulent characteristics of the flow in blade passages of radial pumps and compressor impellers determine the efficiency of these devices. Turbulence is also of great importance for cooling by fluid inside the blades. Depending upon the magnitude of the radial velocity, the Rossby number within rotating machines can range from values close to unity to very small values (≈ 0.05).

Here, we consider a shear flow (free-shear or wall-bounded) of basic velocity, $\bar{\mathbf{u}} = (\bar{u}, 0, 0)$ (x, y, and z are, respectively, the longitudinal, shear, and span-wise directions). We work in a

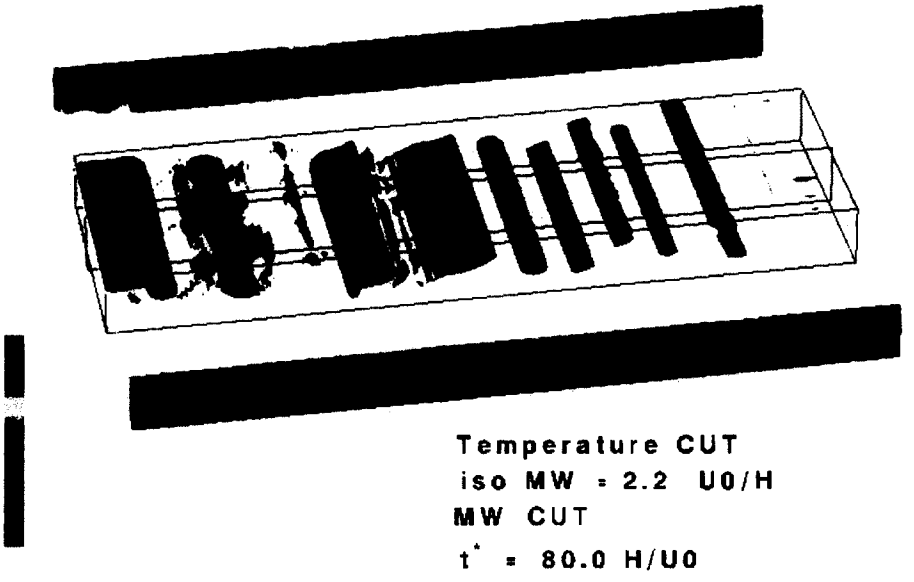

Figure 11 LES (with the SSF model) of a backstep flow in a stably stratified medium; high step ($W/H = 1.25$); $R_i = 0.7$, vorticity and temperature (from Fallon 1994)

frame rotating with a rotation vector $\mathbf{\Omega} = (0, 0, \Omega)$ oriented along the span (positive or negative). The vorticity vector associated with the basic velocity profile $\boldsymbol{\omega} = (0, 0, -\mathrm{d}u/\mathrm{d}y)$ can be parallel or antiparallel to $\mathbf{\Omega}$. We refer to the first case as the cyclonic case, while the second is called anticyclonic. In rotating channel flows, the cyclonic and anticyclonic walls are called, respectively, suction and pressure sides or trailing and leading sides. The effects of rotation on shear flows are drastically different depending on its cyclonic or anticyclonic nature. Laboratory experiments have shown that cyclonic rotation has always a two-dimensionalizing effect. On the cyclonic side of channel flow, as compared to the nonrotating case, the turbulence energy production decreases with increasing rotation rate, and fast rotation can lead to the total suppression of turbulent transition. Conversely, the anticyclonic side is destabilized (three-dimensionalized) for moderate rotation rates (high enough Rossby numbers). Destabilization and stabilization effects are also observed in such rotating free-shear flows as mixing layers, wakes, and jets.

Here, we concentrate on the rotating mixing layer and show, through DNS, how the rotation modifies the 3-D flow topology. The reader is referred to Lesieur et al. (1991), Métais et al. (1992) and Métais et al. (1995) for more details. A solid body rotation does not influence a 2-D flow in a plane perpendicular to the rotation axis, in the sense that the Coriolis force is then proportional to the gradient of the stream function and may be included into the pressure gradient. Therefore, the phenomena observed in the laboratory experiments can only be explained by considering the influence of rotation on the growth of 3-D perturbations.

We consider a temporal mixing layer associated with an hyperbolic-tangent basic velocity profile: $\bar{u}(y) = U_0 \tanh y/\delta$ where $2U_0$ is the velocity difference across the layer, $\delta_i = 2\delta$ being the initial vorticity thickness. The Rossby number is based on the basic vorticity at the inflection point: $R_o^{(i)} = -U_0/2\Omega\delta$. $R_o^{(i)}$ is positive for cyclonic rotation (U_0 and Ω of opposite sign) and negative for anticyclonic rotation.

To describe the early stage of the flow development, a 3-D linear-stability analysis of planar free-shear flows has been carried out by Yanase et al. (1993). For cyclonic rotation and for strong anticyclonic rotation, it was found that the flow was two-dimensionalized, and the instability diagram in the k_x, k_z plane concentrated around the Kelvin–Helmholtz mode (which is not affected by the rotation). For moderate anticyclonic rotation $R_o^{(i)} < -1$, and in addition to the Kelvin–Helmholtz instability, a new instability was discovered consisting of the strong amplification of a purely longitudinal mode.

This linear analysis is, however, limited, since high amplitudes soon develop, and nonlinear interactions develop. In this regime, Lesieur et al. (1991) have emphasized the importance of absolute vorticity stretching, since, in the presence of rotation, Kelvin's theorem applies to it. We recall that absolute vorticity is defined as $\boldsymbol{\omega} + 2\mathbf{\Omega}$. It was, thus, predicted that cyclonic and rapid anticyclonic rotation would inhibit three-dimensionalization and that the longitudinal stretching of absolute vortex lines would be the most efficient in regions were the span-wise absolute vorticity is weak, corresponding to a local Rossby ≈ -1.

To confirm these predictions, we now present DNS at a Reynolds number $\mathrm{Re}^{(i)} = |U_0|\delta/\nu = 50$. Initially, a low-amplitude random noise is superposed upon the basic velocity profiles. Two different types of perturbations are considered. First, a quasi-2-D one consisting of the superposition of a purely 2-D perturbation (z-independent) of kinetic energy $\epsilon_{2D}U_0^2$ and a 3-D perturbation of energy $\epsilon_{3D}U_0^2$, with $\epsilon_{2D} = 10\epsilon_{3D} = 10^{-4}$. The perturbation peaks at the fundamental Kelvin–Helmholtz mode. This case is referred to as the "forced transition" case. The second type of perturbation considered is purely 3-D, with $\epsilon_{3D} = 10^{-4}$ and $\epsilon_{2D} = 0$. The noise is now a white noise which does not favor any mode, and the most amplified one can freely emerge: this case is called the "natural transition" case.

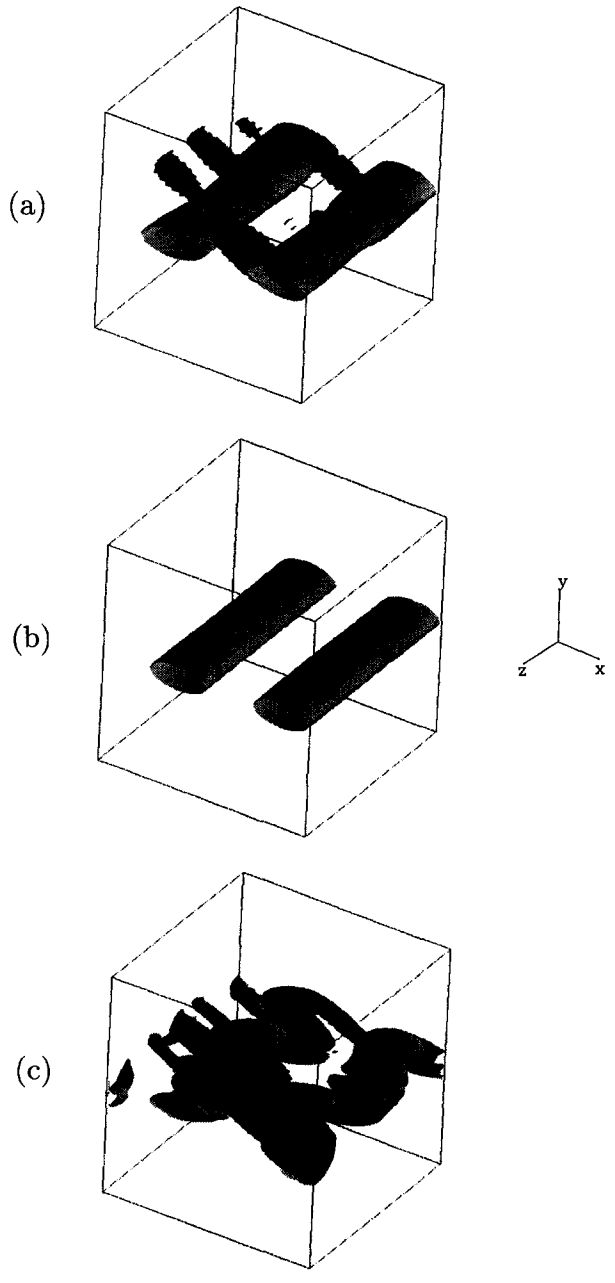

Figure 12 Mixing layer; relative vorticity isosurfaces at $t = 17.8\delta_i/|U_0|$; (a) nonrotating case: ω_z, light gray; ω_l (longitudinal vorticity) colored by the sign of ω_x, black $\omega_x < 0$, dark gray $\omega_x > 0$; (b) $R_o^{(i)} = -1$; (c) $R_o^{(i)} = -5$ (from Métais et al. 1995)

Now we look at the 3-D flow structure in the forced transition case. We focus on the relative vorticity iso-surfaces at $t = 17.8\delta_i/|U_0|$ obtained in the nonrotating case ($R_o^{(i)} = \infty$) and for anticyclonic rotation at $R_o^{(i)} = -5$ and $R_o^{(i)} = -1$.

(1) $R_o^{(i)} = \infty$ (*Figure 12a*). Here, we observe quasi-2-D Kelvin–Helmholtz billows, slightly distorted in the span-wise direction. Weak longitudinal vortices are stretched between the primary rolls: they are visualized through isosurfaces of weak longitudinal vorticity.

(2) $R_o^{(i)} = -1$ (*Figure 12b*) displays the span-wise vorticity field with the same isocontour value as that in the nonrotating case. Anticyclonic and cyclonic flows are similar at this

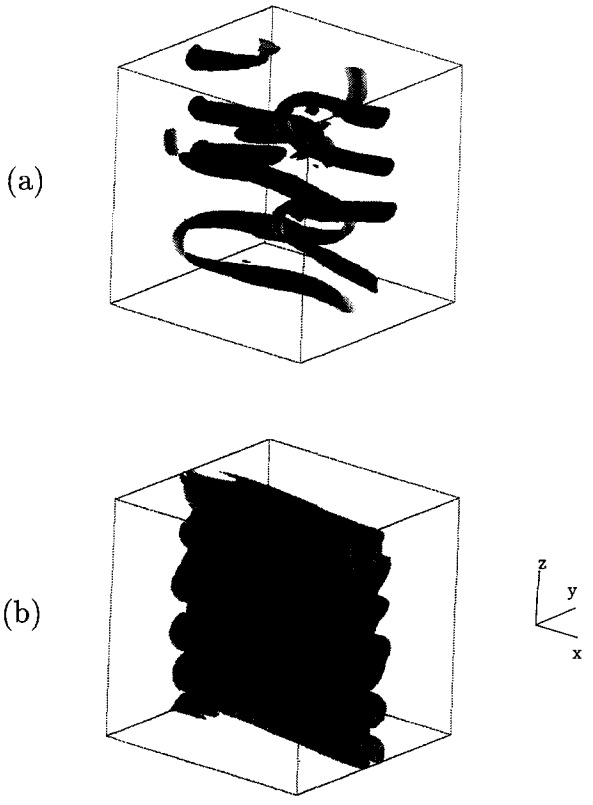

Figure 13 Mixing layer; relative vorticity isosurfaces at $t = 26.8\delta_i / |U_0|$; (a) forced-transition; (b) natural transition; ω_z, light gray; ω_l (longitudinal vorticity) colored by the sign of ω_x; black $\omega_x < 0$; dark gray $\omega_x > 0$

Rossby number, and a strong two-dimensionalization is observed in both cases. The longitudinal vortices have disappeared. Furthermore, the two-dimensionalization tendency can be observed in the cyclonic case even for large positive $R_o^{(i)}$. This agrees well with both the predictions of the linear stability analysis by Yanase et al. (1993).

(3) $R_o^{(i)} = -5$ (*Figure 12c*). Kelvin–Helmholtz vortices are now highly distorted and exhibit strong oscillations along the span-wise direction. The longitudinal vorticity is much higher than in the nonrotating case: we observe the simultaneous formation of Kelvin–Helmholtz vortices and longitudinal hairpin vortices which are stretched between. As time goes on, this produces an important increase of the longitudinal vorticity component: by the end of the run the longitudinal vorticity is approximately twice that associated with the initial mean velocity profile. By the end of the run (*Figure 13a*), the Kelvin–Helmholtz vortices have been totally dislocated, and the flow is entirely composed of hairpin-shaped longitudinal vortices. A similar sequence had been proposed in this case by Lesieur et al. (1991), using the weak absolute vorticity stretching mechanism: weak absolute vorticity in the stagnation region between the Kelvin–Helmholtz rollers would be stretched longitudinally between the latter, yielding longitudinal alternate vortices which should destroy the primary vortices. It is worth noting that these vorticity structures originate from the growth of the longitudinal mode predicted by the linear stability analysis (see Yanase et al. 1993).

The signature of this mode is even clearer when considering the natural transition case. In that case, the linear growth gives initially rise to absolute vortex lines oscillating along the span and in phase in the stream-wise direction. Afterward, we checked that the dynamics are dominated by a strong quasihorizontal stretching of weak *absolute* span-wise vorticity, still corresponding to the phenomenological theory of Lesieur et al. (1991). The isovorticity structures are completely longitudinal in that case (see *Figure 13b*), and exhibit some analogies with the Görtler vortices observed in the boundary layer over a concave wall. Solid body rotation, thus, yields a very efficient mechanism to create intense longitudinal vortices in rotating anticyclonic shear layers, thanks to a linear longitudinal instability followed by a vigorous stretching of absolute vorticity.

Conclusion

The present paper has focused on the dynamics of coherent vortices of various sizes, to which is associated a large part of heat and mass transfers in turbulent flows. Those are studied with 3-D direct or large-eddy simulations. The turbulence considered is either isotropic, or submitted to a stable stratification (within the Boussinesq approximation), an inflectional shear (mixing layers and wakes), a separation, or a solid body rotation.

We first presented the tools of LES for momentum and temperature. We recalled Smagorinsky's model, and introduced Kraichnan's spectral eddy–viscosity and diffusivity, involving a "plateau-cusp behavior." The latter is quite efficient if we can work in Fourier space. However, most industrial applications require to work in physical space. For this purpose, we show how a spectral eddy–viscosity (without cusp) may be implemented in physical space in terms of the second-order structure function of the velocity. This is the (SF) model, which yields very good results for isotropic turbulence. For all these three models (Smagorinsky, spectral cusp, and structure–function) we show that the constant may be adjusted in terms of the Kolmogorov constant, if we assume a Kolmogorov cascade in the subgrid scales. We also present the selective structure–function model, where the eddy–viscosity is turned on only when the flow is sufficiently 3-D, in the sense defined in the paper. We also briefly recall the main lines of the dynamic models, where a double filtering allows to recompute the constant of Smagorinsky's model as a function of space and time.

We discuss the coherent structures of 3-D isotropic turbulence convecting a passive temperature on the basis of DNS. Our simulations confirm earlier findings that these structures consist of thin tubes of high vorticity. We checked that they also correspond to low-pressure regions and that the pressure pdf has exponential-like distribution in the lows, while being Gaussian in the highs. This is related to the highly non-Gaussian wings found in the vorticity components distributions and might characterize the small-scale intermittency of turbulence. We have also found similar types of distributions for a passive temperature convected by the flow. This seems to be associated with an anomalous behavior (with respect to Corrsin–Oboukhov's law) of the scalar spectrum in the energetic scales, with a spectrum close to k^{-1} and a spectral turbulent Prandtl number increasing from 0.3 to 0.6 on the wave number span. All these anomalous temperature effects disappear when a stable stratification, even weak, is activated.

Then, we considered a temporal wake forced by a quasi-2-D perturbation and compared the vortical structure obtained respectively with the structure–function and Smagorinsky's models (no molecular viscosity) and a DNS at the same resolution. In the first two models, longitudinal vortices much more intense than in the DNS are stretched. We also studied with the structure–function model the spatially growing wake and the backward-facing step, and studied the primary and secondary vortex structure. It was shown that the LES preserve both the coherence of the primary vortices (Karman rollers; Kelvin–Helmholtz vortices) and the thin longitudinal hairpin vortices whose diameter is close

to the mesh size. Furthermore, the present computations have demonstrated that LES provide better statistics than the standard $K-\epsilon$ model for separated flows.

The stratified back-step flow, with the top 80% of the inlet channel heated, was also looked at with the structure–function model: increasing the upstream global Richardson number R_i shows how stratification two-dimensionalizes the flow and suppresses longitudinal vortices. We have also carried out at $R_i = 0.7$ a comparison between the structure– and the selective structure–function models. It proves that the latter is much more sensitive to Kelvin–Helmholtz instability and allows for pairings in the early stage of evolution of the layer.

Finally, we studied by DNS the influence of a solid body rotation upon a temporal mixing layer, with the rotation axis parallel to the basic vorticity. The Rossby number R_o is defined with the aid of the vorticity at the inflection point of the initial basic velocity profile, and may be positive (cyclonic rotation) or negative (anticyclonic). For $R_o \geqslant 1$, the mixing layer is two-dimensionalized with respect to the nonrotating case, with a tendency to inhibit the longitudinal hairpin vortex stretching. This is in agreement with linear–stability analysis. For a moderate anticyclonic rotation on the contrary ($R_o = 5$), the mixing layer is disrupted into intense longitudinal alternate filaments of absolute vorticity stretched by the ambient shear.

Contrary to direct numerical simulations, large-eddy simulations are, in principle, not limited to small values of the Reynolds number. Large-eddy simulation techniques have been used for more than 20 years in weather forecasting. More recently, the new subgrid-scale modeling methods, such as those presented in the present paper, combined with the tremendous development of computers have allowed us to demonstrate the applicability of LES to engineering flows. Originally limited to simple flow geometries, LES are now used for spatially growing shear or separated flows, pipe flows, flows around obstacles, and flows submitted to body forces. Both DNS and LES provide deterministic (such as coherent vortices for instance) and statistical information about the flow. They constitute very good tools for assessing the validity of the existing one-point-closure models. Furthermore, they could contribute to the development of a new generation of industrial models incorporating the structural information of the LES.

Acknowledgments

We are indebted to F. Ducros, B. Fallon, C. Flores, M. A. Gonze, D. Grand, J. J. Riley, A. Silveira–Neto, J. Silvestrini, and S. Yanase for numerous contributions to this work or stimulating discussions. We thank also CEA, CNRS, INPG, and UJF for their support. Some of the computations were carried out at the IDRIS (Institut du Développement et des Ressources en Informatique Scientifique, Paris) and at the CGCV (Centre Grenoblois de Calcul Vectoriel).

References

Antonia, R. A., Chambers, A. J., Van Atta, C. W., Friehe, C. A. and Helland, K. N. 1978. Skewness of temperature derivative in a heated grid flow. *Phys. Fluids*, **21**, 509–510

Bardina, J., Ferziger, J. H. and Reynolds, W. C. 1980. Improved subgrid model for large-eddy simulation. AIAA paper 80–1357

Bartello, P., Métals, O. and Lesieur, M. 1994. Coherent structures in rotating three-dimensional turbulence. *J. Fluid Mech.*, **273**, 1–29

Batchelor, G. K., Canuto, C. and Chasnov, J. 1992. Homogeneous buoyancy-generated turbulence. *J. Fluid Mech.*, **235**, 349–378

Champagne, F. H., Friehe, C. A., La Rue, J. C. and Wyngaard, J. C. 1977. Flux measurements, flux estimation techniques, and fine scale turbulent measurements in the surface layer over land. *J. Atmos. Sci.*, **34**, 515–530

Chollet, J. P. and Lesieur, M. 1982. Modélisation sous-maille des flux de quantité de mouvement et de chaleur en turbulence tridimensionnelle isotrope. *La Météorologie VIe Série*, **29** 183–191

Comte, P., Lesieur, M. and Lamballais, E. 1992. Large- and small-scale stirring of vorticity and a passive scalar in a 3-D temporal mixing layer., *Phys. Fluids, A*, **4**, 2761–2778

Comte, P., Ducros, F., Silvestrini, J., David, E., Lamballais, E., Métais, O. and Lesieur, M. 1994. Simulation des grandes échelles d'écoulements transitionnels. *Proc. 14th Fluid Dynamics Symposium on "Application of Direct and Large Eddy Simulation to Transition and Turbulence,"* Chania, Greece, April 1994

David, E. 1993. Modélisation des Ecoulements Compressibles et Hypersoniques: une Approche Instationnaire. Ph.D. thesis, National Polytechnic Institute, Grenoble, France

Deardorff, J. W. 1970. A numerical study of three-dimensional turbulent channel flow at large Reynolds number. *J. Fluid Mech.*, **41**, 453–480

Ducros, F., Comte, P. and Lesieur, M. 1993. Ropes and lambda-vortices in direct and large-eddy simulations of a high Mach number boundary layer over a flat plate. *Turbulent Shear Flows 9*, Kyoto, August 1993 (To appear in the selected proceedings, Springer-Verlag)

Fallon B. 1994. Simulations des Grandes Echelles d'Ecoulements Turbulents Stratifiés en Densité. Ph.D. thesis, National Polytechnic Institute, Grenoble, France

El-Hady, N. M. and Zang, T. A. 1995. Large-eddy simulation of non-linear evolution and break down to turbulence in high-speed boundary layers. *Theor. Comp. Fluid Dynamics*, 7, 217–240

Germano, M. 1992. Turbulence: the filtering approach. *J. Fluid Mech.*, **238**, 325–336

Germano, M., Piomelli, U., Moin, P. and Cabot, W. 1991. A dynamic subgrid-scale eddy–viscosity model. *Phys. Fluids*, **A3** 1760–1765

Gonze M. A. 1993. Simulation Numérique des Sillages en Transition à la Turbulence. Ph.D. thesis, National Polytechnic Institute, Grenoble, France

Jayesh and Warhaft, Z. 1992: Probability distribution, conditional dissipation, and transport of passive temperature in grid-generated turbulence. *Phys. Fluids*, **A4**, 2292–2307

Kraichnan, R. H. 1976. Eddy viscosity in two and three dimensions. *J. Atmos. Sci.*, **33**, 1521–1536

Lele, S. K. 1992. Compact finite difference schemes with spectral-like resolution. *J. Comp. Phys.*, **103**, 16–42.

Lesieur M. 1990. *Turbulence in Fluids*, (2nd ed. rev.), Kluwer, Norwell, MA 412

Lesieur, M. and Herring, J. R. 1985. Diffusion of a passive scalar in two-dimensional turbulence. *J. Fluid Mech.*, **161**, 77–95

Lesieur, M. and Métais, O. 1995. New trends in large-eddy simulations of turbulence. To appear in Ann. Rev. Fluid. Mech.

Lesieur, M. and Rogallo, R. 1989: Large-eddy simulation of passive scalar diffusion in isotropic turbulence. *Phys. Fluids*, **A1** 718–722

Lesieur, M., Yanase, S. and Métais, O. 1991. Stabilizing and destabilizing effects of a solid-body rotation upon quasi-two-dimensional shear layers. *Phys. Fluids*, **A3**, 403–407

Lilly, D. K. 1992. A proposed modification of the Germano subgrid-scale closure method. *Phys. Fluids, A.*, **4**, 633–635

Métais O., Flores C., Yanase S., Riley J. J. and Lesieur M. 1995. Rotating free-shear flows. Part 2: Numerical simulations. *J. Fluid Mech.*, **293**, 47–80

Métais, O. and Lesieur, M. 1992. Spectral large-eddy simulations of isotropic and stably stratified turbulence. *J. Fluid Mech.*, **239**, 157–194

Métais, O., Yanase, S., Flores, C., Bartello, P. and Lesieur, M. 1992. Reorganization of coherent vortices in shear layers under the action of solid-body rotation. In *Turbulent Shear Flows, VIII*, U. Schumann et al. (eds.) Springer-Verlag, 415–430

Moin, P. and Kim., J. 1982. Numerical investigation of turbulent channel flow. *J. Fluid Mech.*, **118**, 341–377

Monin, A. S. and Yaglom, A. M. 1975. *Statistical Fluid Mechanics*, Vol. 2, The MIT Press, Cambridge, MA

Piomelli, U. 1993. High Reynolds number calculations using the dynamic subgrid-scale stress model. *Phys. Fluids*, **A5**, 1484–1490

Saddoughi, S. G. and Veeravalli, S. V. 1994. Local isotropy in turbulent boundary layers at high Reynolds number. *J. Fluid Mech.*, **268**, 333–372

She, Z. S., Jackson, E. and Orszag, S. A. 1990. Intermittent vortex structures in homogeneous isotropic turbulence. *Nature*, **344**, 226

Siggia, E. 1981. Numerical study of small-scale intermittency in three-dimensional turbulence. *J. Fluid Mech.*, **107**, 375–406

Silveira-Neto, A., Grand, D., Métais, O. and Lesieur, M. 1991. Large-eddy simulation of the turbulent flow in the downstream region of a backward-facing step. *Phys. Rev. Lett.* **66**, 2320–2323

Silveira-Neto, A., Grand, D., Métais, O. and Lesieur, M. 1993. A numerical investigation of the coherent vortices in turbulence behind a backward-facing step. *J. Fluid Mech.*, **256**, 1–25

Silvestrini, G., Comte, P. and Lesieur, M. 1995. DNS and LES of incompressible mixing layers developing spatially. *Proc. 10th Symposium on Turbulent Shear Flows*, The Pennsylvania State University, August 1995

Smagorinsky, J. 1963. General circulation experiments with the primitive equations. *Monthly Weather Rev.*, **91**, 99–164

Sreenivasan, K. R., Tavoularis, S., Henry, R. and Corrsin, S. 1980. Temperature fluctuations and scales in grid-generated turbulence. *J. Fluid Mech.*, **100**, 597–621

Staquet, C. 1991. Influence of a shear on a stably stratified flow. In *Turbulence and Coherent Structures*, O. Métais and M. Lesieur (eds.), Kluwer Academic Publishers, Norwell, MA, 469–487

Thoroddsen, S. T. and Van Atta, C. W. 1992. Exponential tails and skewness of density-gradient probability density functions in stably stratified turbulence. *J. Fluid. Mech.* **244**, 547–566

Vincent, P. and Meneguzzi, M. 1991. The spatial structure and statistical properties of homogeneous turbulence. *J. Fluid Mech.*, **225**, 1–20

Yakhot, V. and Orszag, S. 1986 Renormalization Group (RNG) methods for turbulence closure. *J. Scientific Computing*, **1**, 3–52

Yanase, S., Flores, C., Métais, O. and Riley, J. J. 1993. Rotating free-shear flows. I. Linear stability analysis. *Phys Fluids*, **A5**, 2725–2737

Zang, Y., Street R. L. and Koseff J. R. 1993. A dynamic mixed subgrid scale model and its application to turbulent recirculating flows. *Phys. Fluids*, **5**, 3186–3196